crystals

MDPI

*Article*

# Natural Forsterite Strongly Enriched in Boron: Crystal Structure and Spectroscopy

**Bijie Peng [1], Mingyue He [1,*], Mei Yang [2], Shaokun Wu [1] and Jingxin Fan [1]**

[1] School of Gemmology, China University of Geosciences, Beijing 100083, China; pengbijie@163.com (B.P.); 3009210005@email.cugb.edu.cn (S.W.); 2009210011@email.cugb.edu.cn (J.F.)
[2] Sciences Institute, China University of Geosciences, Beijing 100083, China; yangmei@cugb.edu.cn
* Correspondence: hemy@cugb.edu.cn

**Abstract:** Boron is a typical crustal element and largely incompatible in olivine. Most natural olivine samples have very low concentrations of boron. Recently, forsterite with high boron content (up to 60.53 wt% MgO and 1795.91 ppm B) has been discovered in the Jian forsterite jade in the Jian area of northeast China. In this study, B-rich forsterite was examined by electron microprobes, Laser Ablation-Inductively Coupled Plasma Mass Spectrometry, Single crystal X-ray diffraction, Raman spectroscopy, and infrared spectroscopy. The B-rich forsterite is orthorhombic, existing in space group *Pnma*, and its unit-cell parameters are: a = 10.1918(7) Å, b = 5.9689(4) Å, c = 4.7484(3) Å, α = 90°, β = 90°, γ = 90°, and V = 288.86(3) Å$^3$. The results of single crystal X-ray diffraction analysis indicate that the unit-cell parameters (a, b, and c) and unit-cell volume of forsterite in Jian forsterite jade are much smaller than those of known olivine. An equivalent set of Raman and infrared spectra were measured for the natural B-rich forsterite and compared to the results for mantle forsterite with a Fo value of ~91. The Raman spectrum of B-rich forsterite is similar to that of mantle olivine. We conclude that the systematic peak position shifts towards higher Raman shift with increasing Fo content. The infrared spectrum of B-rich forsterite crystals is characterized by strong absorption bands at 761, 1168, 1259, and 1303 cm$^{-1}$, which are assigned to stretching vibrations of $BO_3$ groups. Our data further confirm the existence of the B(F, OH)$Si_{-1}O_{-1}$ coupled substitution in natural B-rich forsterite.

**Keywords:** forsterite; boron; crystal structure; spectroscopy



**Citation:** Peng, B.; He, M.; Yang, M.; Wu, S.; Fan, J. Natural Forsterite Strongly Enriched in Boron: Crystal Structure and Spectroscopy. *Crystals* **2022**, *12*, 975. https://doi.org/10.3390/cryst12070975

Academic Editor: Carlos Rodriguez-Navarro

Received: 21 June 2022
Accepted: 11 July 2022
Published: 12 July 2022



## 1. Introduction

Olivine is one of the simplest silicate minerals, and the general crystal chemical formula of which is $(A)_2SiO_4$, where A—$Mg^{2+}$, $Fe^{2+}$, $Mn^{2+}$, etc. The olivine crystal structure is orthorhombic with a slightly distorted hexagonal close packing array of oxygen atoms. Si is on tetrahedral interstices and Mg and Fe ions are on octahedral sites (labeled M1 and M2). The M1 site is a distorted octahedra at the center of symmetry whereas M2 is a regular octahedra on the mirror plane [1–4]. Olivine is a general name of forsterite-fayalite sold solution [5]. In addition to the complete isomorphism of Mg and Fe, olivine also contains some petrogenetically significant minor components, such as B, Li, Co, P, and As [4,6,7].

A growing body of crystal structure and spectroscopy investigations have been carried out on both synthetic and natural olivine over the past few years. The majority of the previous studies have primarily focused on crystal structure refinement [3,4,8,9], the effect of temperature and pressure on the crystal structure [10–14], the chemical composition of the forsterite-fayalite series determination [15,16], residual pressure calculation [17], and water content estimation [18]. Although extensive studies have been conducted on olivine over a range of compositions, temperatures, and pressures using a variety of methods, more research is needed on several aspects of the properties of B-rich olivine.

Boron is a typical crustal element with high concentrations in rocks closely related to continents and rocks interacting with the hydrosphere, but low concentrations in mantle

peridotite [19,20]. B-rich olivine, associated with clinohumite K-rich pargasite, uvite, spinel, magnetite, ludwigite, and sinhalite, was first described from the Tayozhnoye Fe deposit of Russia [21]. Sykes et al. [22] studied the infrared spectrum and transmission electron microscopy of B-rich olivine and presented the first direct evidence of coupled substitution of boron and hydrogen for silicon. More precise and complex coupled substitution mechanisms were presented by Kent and Rossman [6] and Gose et al. [23]. More recently, Ingrin et al. [24] identified the position of the OH bands associated with the boron substitution through the infrared spectrum. Unfortunately, due to the incompatibility of boron in olivine, the connection between boron and olivine is often neglected. Hence, we addressed the key question: Whether the incorporation of B in olivine will affect the structure of olivine? Whether the Raman spectrum and infrared spectrum of boron-containing olivine be different from those of boron-free olivine? Additionally, most previous studies on the B-contained olivine were performed on synthetic olivine. Therefore, it is inevitable to investigate the properties of natural B-rich olivine.

In this paper, we report a new occurrence of natural end-member forsterite in Jian forsterite jade from Jilin province, China. Besides the high content of Mg, this forsterite has another unusual feature, namely strong enrichment by B. We present chemical composition, single crystal X-ray diffraction, Raman spectrum, and infrared spectrum studies for B-rich forsterite. Our results refine the crystal structure of B-rich forsterite and provide strong evidence for the coupled substitution of H and B for Si in natural B-rich forsterite. This study presents a basis for understanding the formation of natural B-rich forsterite.

## 2. Materials and Methods

The natural B-rich forsterite crystals, directly selected from the Jian forsterite jade, were used for detailed data analyses. The Jian forsterite jade is a new type of jade that has been recently found in the Jian area of northeast China [25]. It is mainly composed of forsterite, serpentine, and brucite (Figure 1a,b). We crushed the jade to 60–80 mesh, and hand-picked crack-free and inter-transparent olivine particles under binoculars for analysis. The size of the selected forsterite is 0.3–1 mm (Figure 1c,d). Forsterite with Fo~91 in mantle peridotite xenolith from Jilin province, China was chosen for comparison (Sample O-1 and O-2).

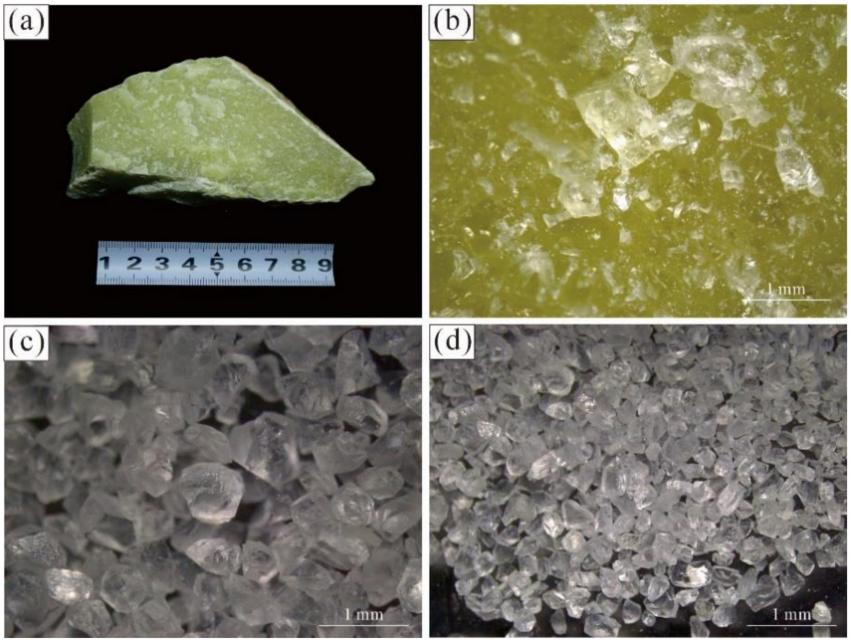


**Figure 1.** Sample photographs. (**a**) the Jian forsterite jade. (**b**) 40× magnification observation of (**a**) under gem microscope. (**c**) and (**d**) hand-picked B-rich forsterite.

The chemical compositions of forsterite were obtained on polished thin sections using an EPMA-1720 electron microprobe at the Electron Probe Laboratory, China University of Geosciences (Beijing, China). The primary analyzing settings were a 5 μm beam spot diameter, 10 nA beam, and 15 kV acceleration voltage. The standards used to calibrate the electron microprobe were 52 standard minerals from the SPI Company of the United States, Washington, DC, USA.

In situ trace element analyses were carried out at the Mineral Laser Microprobe Analysis Laboratory (Milma Lab, Beijing, China), China University of Geosciences (Beijing) using Laser Ablation-Inductively Coupled Plasma Mass Spectrometry (LA-ICP-MS). An Agilent 7900 ICP–MS fitted with a NewWave 193UC excimer laser ablation system was used. A laser repetition rate of 8 Hz at 3 J/cm$^3$ and a spot diameter of 50 μm were used in the analyses. NIST 610 was used as the external standard, Si was used as the internal standard, and ARM-1 and BCR-2G were used as the monitoring standards.

Single crystal X-ray diffraction measurements were obtained at ambient conditions with a Rigaku Xtalab PRO diffractometer system and HyPix-6000HE detector at the Laboratory of X-ray single crystal diffraction, China University of Geosciences (Beijing). The experiment was conducted with φ and Ω scanning mode, and the scanning step size was 0.5. Monocrystalline silicon array was used to conduct monochromatic processing on the wavelength, and X-ray (λ = 0.71073 Å) was used as the diffraction source to collect diffraction data. A 1.2 Kw water cooled microfocus source with a Mo rotor target and multilayer mirrors were used to collect intensity data. The atomic coordinates of samples are provided as CIF files in the Supplementary Materials. COD (entries 3000401) contains the supplementary crystallographic data for this paper.

The Raman spectrum was obtained using a Horiba HR-Evolution Raman microspectrometer with an Ar-ion laser operating at 532 nm excitation at the School of Gemmology, China University of Geosciences (Beijing). A 100 μm entrance slit and a grating with 1200 grooves per mm were used to collect the scattered light. Every Raman spectrum was acquired by 10 scans with 1 cm$^{-1}$ resolution in the 4000–100 cm$^{-1}$ range.

The infrared spectrum was obtained using the Tensor 27 Fourier infrared spectrometer at the School of Gemmology, China University of Geosciences (Beijing). All sample analyses adopted the transmission method. The experimental test conditions were as follows: test voltage was 220 V, the resolution was 4 cm$^{-1}$ with 64 scans, the scanning range was 4000–400 cm$^{-1}$, and the scanning speed was 10 kHz.

## 3. Results

### *3.1. EPMA*

The chemical composition of olivine is end-member forsterite. All tested samples are compositionally homogeneous. The characteristics of zonation or exsolution lamellae are not observed. The Forsterite is Mg-rich (MgO > 57 wt%), and Fe-poor (FeOtot < 1 wt%). The Fo (100 × Mg/[Mg + Fe], mol%) of forsterite varies from 99.62 to nearly 99.74. The NiO content of this olivine is very low (<0.08 wt%), and the CaO content varies between 0.01 and 0.04 wt%. In addition, forsterite contains a certain amount of fluorine (0.13–1.06 wt%). Olivine in mantle peridotite xenolith is relatively iron-rich with Fo values of ~91. The content of NiO and CaO is higher than that of end-member forsterite. The chemical compositions are listed in Table 1.

**Table 1.** Chemical composition of B-rich forsterite and mantle olivine.

| Sample | S-1 | S-2 | S-3 | S-4 | O-1 | O-2 |
|---|---|---|---|---|---|---|
| $SiO_2$ | 39.41 | 41.98 | 41.84 | 41.71 | 41.31 | 41.33 |
| $TiO_2$ | 0.12 | 0.05 | 0.02 | 0.03 | 0.00 | 0.00 |
| $Al_2O_3$ | 0.03 | 0.01 | 0.02 | 0.01 | 0.00 | 0.00 |
| $Cr_2O_3$ | 0.00 | 0.00 | 0.00 | 0.00 | 0.02 | 0.00 |
| FeO | 0.28 | 0.37 | 0.35 | 0.39 | 8.17 | 7.86 |

**Table 1.** *Cont.*

| Sample | S-1 | S-2 | S-3 | S-4 | O-1 | O-2 |
|---|---|---|---|---|---|---|
| MnO | 0.04 | 0.01 | 0.08 | 0.00 | 0.06 | 0.15 |
| NiO | 0.08 | 0.00 | 0.05 | 0.00 | 0.44 | 0.36 |
| MgO | 60.53 | 58.21 | 57.12 | 57.20 | 49.54 | 49.74 |
| CaO | 0.04 | 0.00 | 0.01 | 0.01 | 0.021 | 0.03 |
| $Na_2O$ | 0.00 | 0.00 | 0.01 | 0.03 | 0.00 | 0.00 |
| $K_2O$ | 0.01 | 0.00 | 0.02 | 0.03 | 0.00 | 0.00 |
| F | 1.06 | 0.13 | 0.17 | 0.18 | 0.00 | 0.00 |
| Total | 101.59 | 100.75 | 99.69 | 99.59 | 99.55 | 99.47 |
| Fo | 99.74 | 99.64 | 99.66 | 99.62 | 91.53 | 91.86 |

### *3.2. LA-ICP-MS*

The main trace element feature of the end-member forsterite is the extremely high content of B (1773.4–1795.91 ppm) (Figure 2). The content of compatible elements Cr, Co, and Ni is depleted. The concentrations of other trace elements are relatively low. Li and Ti concentrations range from 1.93 to 2.62 and 4.17 to 9.61 ppm, respectively. Other elements do not show any notable characteristics. The distribution of trace elements in olivine is very uniform [25]. Detailed trace elements contents are listed in Table 2. The trace element characteristics of B-rich forsterite are different from those of common mantle peridotite [26].

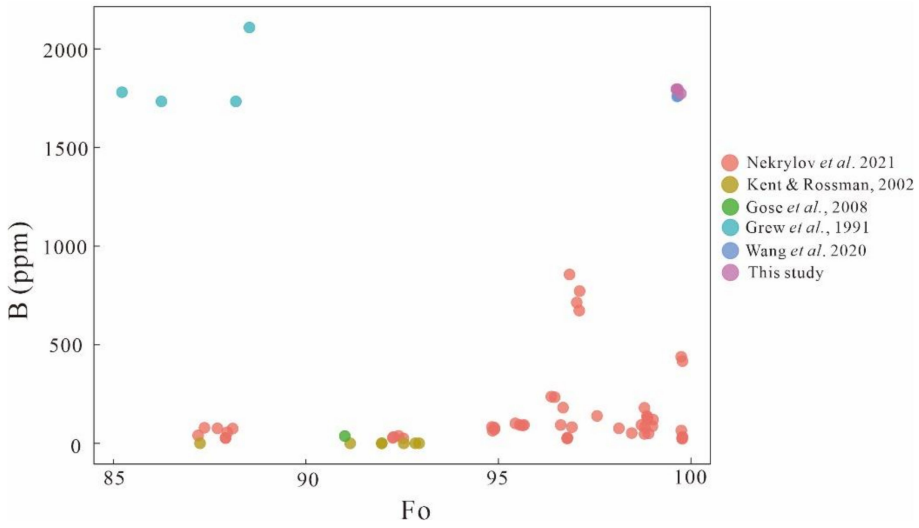


**Figure 2.** The B concentration of forsterite from the Jian forsterite jade compared with olivine from other origins.

**Table 2.** Trace element composition (ppm) of B-rich forsterite.

| Element | S-1 | S-2 | S-3 | S-4 | O-1 | O-2 |
|---|---|---|---|---|---|---|
| Li | 1.93 | 2.17 | 2.51 | 2.62 | 1.18 | 1.05 |
| B | 1773.4 | 1792.54 | 1795.56 | 1795.91 | b.d.l. | b.d.l. |
| Na | b.d.l. [1] | b.d.l. | b.d.l. | b.d.l. | 92 | 90 |
| Al | 37.82 | 43.16 | 45.21 | 48.94 | 27 | 23 |
| P | 118.2 | 120.18 | 135.78 | 142.24 | 38 | 43 |
| Ca | b.d.l. | b.d.l. | b.d.l. | b.d.l. | 74 | 58 |
| Sc | 1.22 | 1.247 | 1.249 | 1.25 | 0.58 | 0.76 |
| Ti | 9.58 | 6.51 | 9.61 | 4.17 | 165 | 35 |
| V | 0.587 | 0.609 | 0.614 | 0.654 | 3.8 | 2.9 |
| Cr | b.d.l. | b.d.l. | b.d.l. | b.d.l. | 88 | 102 |
| Mn | 200.71 | 201.72 | 203.69 | 210.69 | 610 | 636 |
| Co | 0.592 | 0.594 | 0.604 | 0.613 | 127 | 121 |

**Table 2.** *Cont.*

| Element | S-1 | S-2 | S-3 | S-4 | O-1 | O-2 |
|---|---|---|---|---|---|---|
| Ni | 0.914 | 0.928 | 0.944 | 0.974 | 2890 | 2868 |
| Cu | b.d.l. | b.d.l. | b.d.l. | b.d.l. | 1.52 | 1.10 |
| Zn | 43.92 | 43.96 | 45.49 | 46.34 | 56 | 42 |
| Ga | 0.271 | 0.29 | 0.3 | 0.301 | b.d.l. | b.d.l. |
| Sr | b.d.l. | b.d.l. | b.d.l. | b.d.l. | b.d.l. | b.d.l. |
| Y | 0.0675 | 0.07 | 0.0736 | 0.0738 | 0.02 | b.d.l. |
| Zr | 1.002 | 1.134 | 1.148 | 1.95 | 0.21 | 0.19 |
| Nb | 0.119 | 0.1232 | 0.1392 | 0.146 | 0.26 | 0.015 |
| Ce | b.d.l. | b.d.l. | b.d.l. | b.d.l. | b.d.l. | b.d.l. |

[1] b.d.l., Below the detected line.

### *3.3. Single Crystal X-ray Diffraction*

Crystal data for B-rich forsterite: orthorhombic, space group *Pnma*, a = 10.1918(7) Å, b = 5.9689(4) Å, c = 4.7484(3) Å, $\alpha$ = 90°, $\beta$ = 90°, $\gamma$ = 90°, and V = 288.86(3) Å$^3$, Z = 4, T = 293(2)K, $\mu$(MoK$\alpha$) = 1.16 mm$^{-1}$, Dcalc = 3.25 g/cm$^3$, 3161 reflections measured (7.998° $\leq 2\Theta \leq$ 60.592°), 439 unique (Rint = 0.0824, Rsigma = 0.0500) which were used in all calculations. The final R1 was 0.0350 (I > 2$\sigma$(I)) and wR2 was 0.0948 (all data). In the crystal structure of forsterite, each structure unit contains one Si site, two cation sites, and three O sites (Figure 3). All the silicon atoms are coordinated to four oxygen atoms to form [$SiO_4$] tetrahedrons and account for one-eighth of tetrahedral voids. Isolated [$SiO_4$] tetrahedron (T) is surrounded by [$MgO_6$] octahedra (M1 and M2). The Si–O bond distances vary from 1.613(3) to 1.6312(14) Å (Table 3). The average O–Si–O bond angle is 109.15°. As shown in Figure 3, magnesium atoms are coordinated with six oxygen atoms to form [$MgO_6$] octahedra. Two cation M sites M(1) and M(2) are occupied by magnesium atoms. The M(1) site is located at the center of symmetry, while the M(2) site is located on the mirror plane. The Mg1–O bond distances vary from 2.0622(14) to 2.1283(14) Å and the Mg2–O bond distances from 2.049(3) to 2.2068(16) Å. The O–Mg–O angles vary from 71.65(8)° to 109.93(9)° (Table 3). Table 3 shows bond distances and angles parameters for M1, M2, and T.

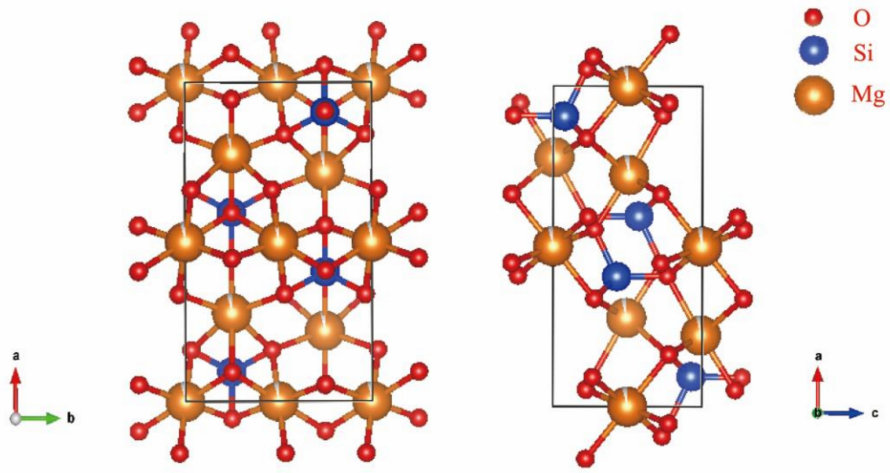


**Figure 3.** Unit-cell of B-rich forsterite structure viewed along c and b axes.

Compared with published olivine cell parameters [3,8,13,27–30], B-rich forsterite tested in this study shows the smallest unit cell parameters (Figure 4). As shown in Figure 4a–c, a negative and significant correlation between unit-cell parameters and the Fo value, which is in agreement with the results of Princivalle and Secco [3]. The parameter a is most affected by compositional changes ($1/k_a > 1/k_b > 1/k_c$). Figure 4d–f show that cell volume and coordination polyhedron volume of tested forsterite are both inversely proportional to

magnesium contents. Figure 4g,h show the shortening of M1–O, and M2–O bond distances with increasing magnesium contents.

**Table 3.** Bond distances (Å) and bond angles of B-rich forsterite.

| | Bond Distance/Å | Bond Angle |
|---|---|---|
| octahedra M1 | (Mg1–O1)[2] = 2.0622(14) Å<br>(Mg1–O2)[2] = 2.0816(16) Å<br>(Mg1–O3)[2] = 2.1283(14) Å<br><br>Average 2.0907 | (O3–Mg1–O2) = 85.02(7)<br>(O2–Mg1–O1) = 86.53(7)<br>(O2–Mg1–O3) = 94.98(7)<br>(O2–Mg1–O1) = 93.47(7)<br>(O3–Mg1–O2) = 94.98(7)<br>(O1–Mg1–O2) = 93.47(7)<br>(O3–Mg1–O2) = 85.02(7)<br>(O1–Mg1–O2) = 86.53(7)<br>(O1–Mg1–O3) = 105.06(7)<br>(O3–Mg1–O1) = 105.06(7)<br>(O3–Mg1–O1) = 74.94(7)<br>(O3–Mg1–O1) = 74.94(7)<br>Average 90 |
| octahedra M2 | (Mg2–O1)[1] = 2.049(3) Å<br>(Mg2–O2)[1] = 2.175(3) Å<br>(Mg2–O3)[2] = 2.2068(16) Å<br>(Mg2–O3′)[2] = 2.0674(14) Å<br><br>Average 2.1286 | (O1–Mg2–O3) = 96.76(7)<br>(O3–Mg2–O3) = 88.83(4)<br>(O3–Mg2–O2) = 80.97(7)<br>(O3–Mg2–O3) = 71.65(8)<br>(O1–Mg2–O3) = 90.79(6)<br>(O3–Mg2–O3) = 109.93(9)<br>(O2–Mg2–O3) = 90.82(6)<br>(O3–Mg2–O3) = 88.83(4)<br>(O1–Mg2–O3) = 90.79(6)<br>(O3–Mg2–O2) = 90.82(6)<br>(O2–Mg2–O3) = 80.97(7)<br>(O1–Mg2–O3) = 96.76(7)<br>Average 89.83 |
| tetrahedron T | (Si–O3) = 1.6312(14) Å<br>(Si–O1) = 1.656(3) Å<br>(Si–O2) = 1.613(3) Å<br>(Si–O3) = 1.6312(14) Å<br><br>Average 1.6327 | (O3–Si–O2) = 116.09(7)<br>(O2–Si–O1) = 114.46(11)<br>(O1–Si–O3) = 101.75(7)<br>(O3–Si–O3) = 104.72(11)<br>(O2–Si–O3) = 116.09(7)<br>(O1–Si–O3) = 101.75(7)<br>Average 109.15 |

Numbers in square brackets represent the number of repeats of bonds and bond angles in a polyhedron.

### *3.4. Raman Spectrum*

Laser Raman spectroscopy is a powerful method for structural and compositional characterization of minerals. The factor group analysis indicates that forsterite has 36 Raman-active vibration modes: $11A_g + 11B_{1g} + 7B_{2g} + 7B_{3g}$ [31,32]. Symmetry and assignment for the Raman modes of B-rich forsterite are listed in Table 4. A Raman spectrum of B-rich forsterite can be divided into three spectrum regions: (1) 700–1100 $cm^{-1}$, (2) 400–700 $cm^{-1}$, and (3) < 400$cm^{-1}$ [15]. The bands of the region (1) (at approximately 824, 857, 882, 919, and 965 $cm^{-1}$ for B-rich forsterite) are attributed to the internal symmetric and asymmetric stretching vibrational modes of the $SiO_4$ ionic group [15]. Bands between 700 and 1100 $cm^{-1}$ are the most characteristic peak of the olivine Raman spectrum, which can be used to identify olivine in the multi-phase spectrum [15,16,31]. Low intense bands of the region (2) (at 437, 544, 586, and 609 $cm^{-1}$ for B-rich forsterite) are related to the internal bending vibrational modes of the $SiO_4$ ionic groups [15]. The bands of the region (3) (at around 227, and 305 $cm^{-1}$ for B-rich forsterite) are assigned to the lattice vibration modes, including rotational and translational vibrations of $SiO_4$ tetrahedra, and translational vibrations of magnesium and iron cations [31]. In addition, bands associated with the vibration of B-O

are not detected, which is attributed to the concentration of boron. Generally speaking, boron has no effect on the Raman spectra of olivine.

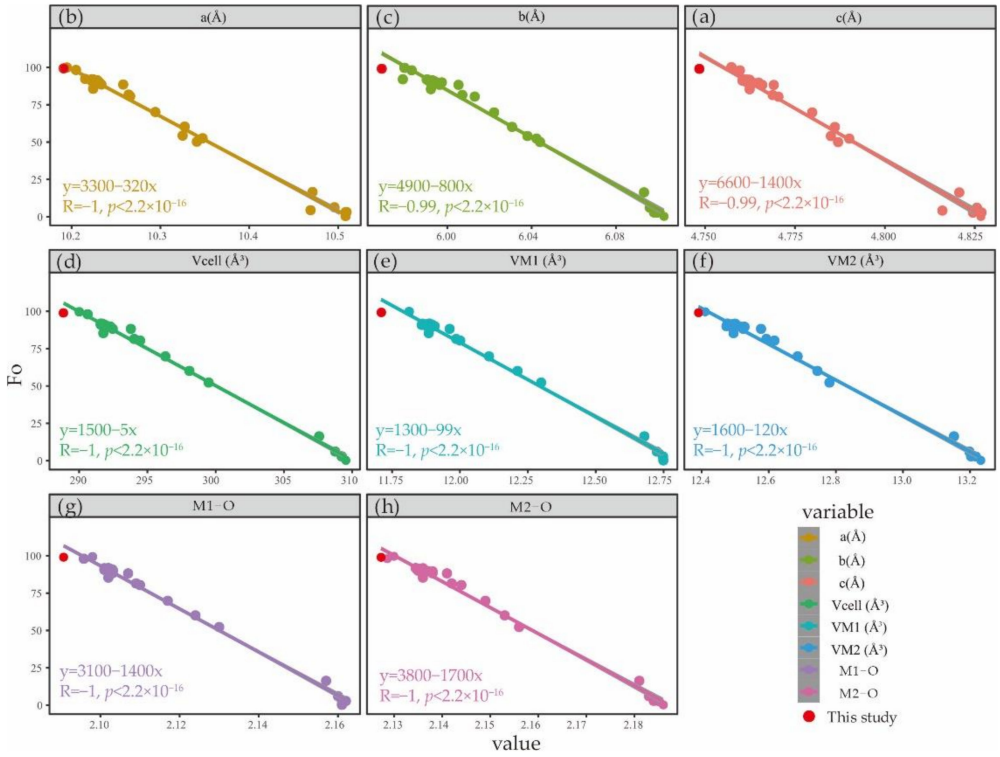


**Figure 4.** (**a**–**c**) Unit-cell parameters **a**, **b**, **c** vs. Fo content of olivine. (**d**) Unit-cell volume vs. Fo content of olivine. (**e**,**f**) The volume of coordination polyhedron M1, and M2 vs. Fo content of olivine. (**g**,**h**) Average M1–O, and M2–O bond distances vs. Fo content of olivine.

**Table 4.** Assignment of bands in the Raman spectrum of the forsterite.

| Band ($cm^{-1}$) | | Symmetry | Assignment |
|---|---|---|---|
| **B-Rich Olivine (Fo = 99)** | **B-Free Olivine (Fo = 91)** | | |
| 227 | 220 | $A_g$ | $SiO_4$ translation |
| 305 | 300 | $A_g$ | $M_2$ translation |
| 437 | 433 | $B_{1g}$ | $v_2$ |
| 544 | 540 | $A_g$ | $v_4$ |
| 586 | 581 | $B_{2g}$ | $v_4$ |
| 609 | 603 | $A_g$ | $v_4$ |
| 824 | 820 | $A_g$ | $v_1 + v_3$ |
| 857 | 852 | $A_g$ | $v_1 + v_3$ |
| 882 | 878 | $B_{2g}$ | $v_3$ |
| 919 | 916 | $B_{3g}$ | $v_3$ |
| 965 | 958 | $A_g$ | $v_3$ |

In our analysis, another feature of the Raman spectrum is that the systematic peak position shift towards higher Raman shift compared with Fo~91 olivine (820, 852 for Fo~91 olivine and 824, 857 for Fo~99 olivine, respectively) (Figure 5b). The behavior of atomics at the M2 octahedral site is the main factor affecting the Raman spectrum of olivine [33]. Our results indicate that the relative intensities and position of the Raman peak in olivine can be correlated with the type of atomic substitutions involved. Kuebler et al. [15] explained that systematic peak-position is related to the decrease in atomic mass and polyhedral volume in octahedral sites, and to the degree of coupling of the symmetric and asymmetric stretching vibrational modes of $SiO_4$ groups.

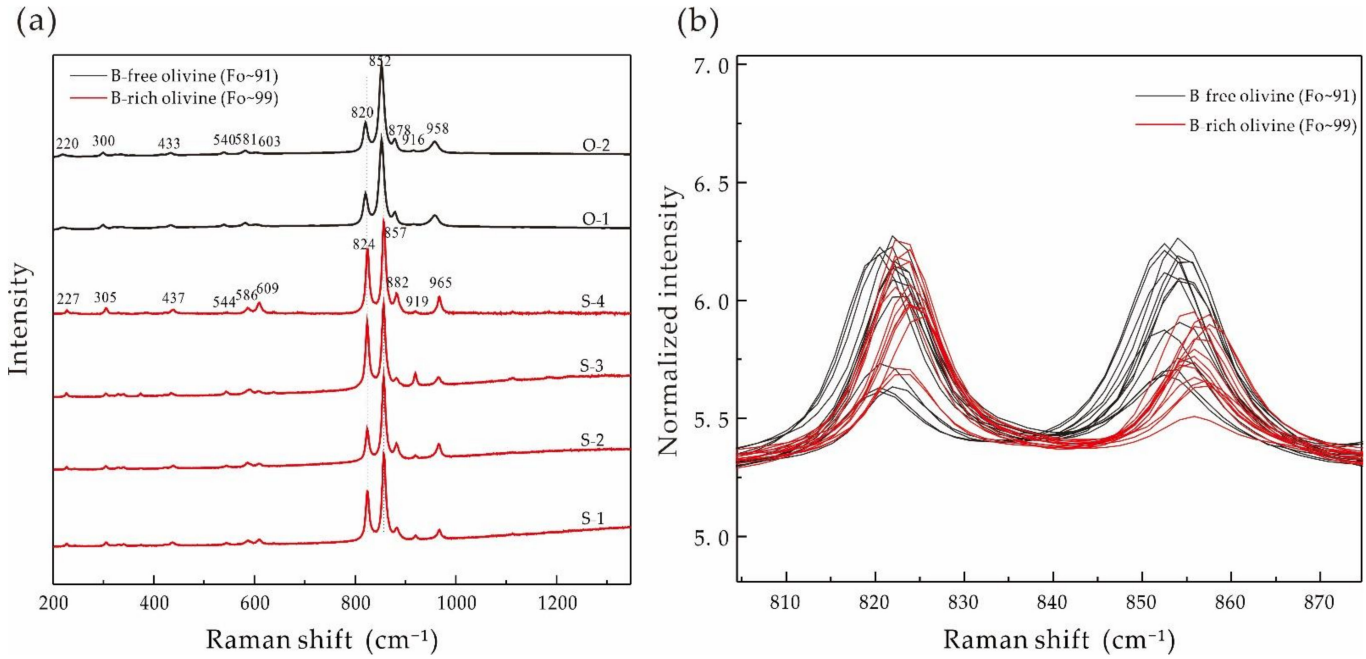


**Figure 5.** Raman spectrum of B-rich forsterite compared with mantle olivine. (**a**) The Raman spectrum of samples. (**b**) The magnification of (**a**).

### *3.5. Infrared Spectrum*

The characteristic peaks of B-rich forsterite appear mainly at approximately 1303, 1259, 1168, 990, 958, 883, 839, 761, 610, 508, 468, and 424 $cm^{-1}$. The bands around 990, 958, and 883 $cm^{-1}$ are related to the symmetrical stretching vibration of the Si−O−Si group. The bands near 468, 508, and 610 $cm^{-1}$ represent the bending vibration of the Si−O group. Internal vibrations and lattice vibrations appear at 468 and 424 $cm^{-1}$. The IR spectrum of B-rich forsterite displays strong OH band at 3696 $cm^{-1}$ and weaker band at 3593 $cm^{-1}$. Both bands are caused by OH stretching vibration, which indicates the existence of constitutional water in forsterite.

Figure 6 compares the IR spectra of B-rich forsterite from Jian forsterite jade and B-free olivine (Fo~91) from mantle peridotite. The spectra are similar, except for five bands at 761, 1168, 1259, 1303, and 3593 $cm^{-1}$ in the spectrum of the B-rich forsterite. Similar bands have been reported in B-rich olivine samples [22,24]. The band at 761 $cm^{-1}$ is close to the 758 $cm^{-1}$ band observed in the infrared spectrum of B-rich olivine from Tayozhnoye, Russia. Sykes et al. [22] assigned the band at 758 $cm^{-1}$ to the $v_1$ symmetric stretching mode of the $BO_3$ groups. The bands at 1168 and 1259 $cm^{-1}$ in the B-rich forsterite spectra are assigned to $\nu_3$ asymmetric stretching vibration modes of $BO_3$ groups [22,24]. The bands at 1301 $cm^{-1}$ likely correspond to the isotopic shift of the bands at 1168 and 1256 $cm^{-1}$, respectively, due to $^{10}B$ [24].

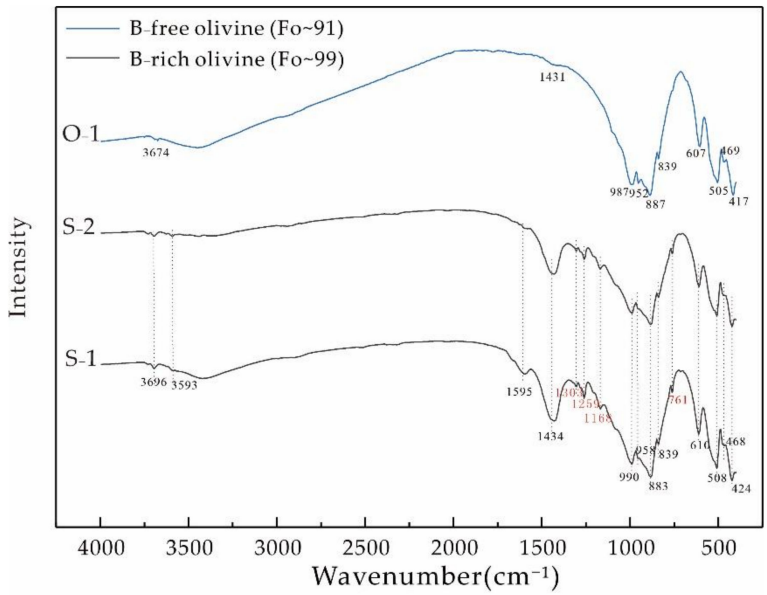


**Figure 6.** The infrared spectrum of B-rich forsterite compared with mantle olivine.

## 4. Discussion

### *4.1. The Coupled Substitution B(F, OH)$Si_{-1}$, $O_{-1}$*

The incorporation of boron in olivine is mainly related to the coupled substitution of boron and H for silicon [6,21–24]. The $BO_3$ group lies on the (O3−O1−O3) face of the tetrahedral site, inclined at 17° from the (x,y) plane, and the H atom is bonded to the O2 atom [24]. The O2−H group points either to the O1 oxygen or out of the tetrahedral site. The former configuration is more stable than the latter [24]. The introduction of B promotes the formation of defects in the crystal structure of forsterite and may result in a distortion of the tetrahedral site [22,34], which is interpreted as the formation of terminal B−(OH) or B−F bonds or the perturbation of the B−O−M linkage. Guo et al. [35] pointed out that the substitution of B for Si may result in the reduction in cell parameters and cell volume of forsterite.

The results of single crystal X-ray diffraction analysis indicate that the unit-cell parameters (a, b, and c) and unit-cell volume of forsterite in Jian forsterite jade are much smaller than those of known olivine. The small crystal parameters are rather due to an increased content of Mg. It's well known that lattice parameters linearly decrease with increasing forsterite [3]. However, we compared the lattice parameters of B-rich forsterite (Fo = 99.7) with pure forsterite (Fo = 100) (Figure 4) [1,13]. The lattice parameters of the former are smaller than those of the latter. Similar phenomena were described in B-rich diopside [34]. Halenius et al. [34] presented that a B−Si substitution in B-rich diopside decreases the T site volume and leads to disruption of one of the T−O bonds compared with end-member diopside. In our study, $V_T$ (Å$^3$) in B-rich forsterite (2.196 Å$^3$) is smaller than that of pure forsterite (2.21 Å$^3$). Thus, we speculated that the incorporation of B in olivine slightly reduces the lattice parameters, especially decreases the T site volume and affects the neighboring M1 and M2 sites. Due to the low concentration of B, the X-ray diffraction techniques can't resolve the true coordination of B in forsterite. Nevertheless, the occurrence of the $BO_3$ group is further demonstrated by our spectra data.

B incorporation into forsterite has no effect on the Raman spectrum. In our study, the difference between B-rich and B-free forsterite Raman spectrum is caused by the different magnesian contents. No evident bands of B−O vibration appear in the Raman spectrum. While significant differences are observed between the B-rich and B-free forsterite IR spectrum. B-rich forsterite displays extra five bands at 761, 1168, 1259, 1303, and 3593 cm$^{-1}$ compared with B-free forsterite. The vibrational bands at 1200–1400 cm$^{-1}$ are related to B–O vibrations [22,24,34]. Halenius et al. [34] reported the existence of the replacement

of $SiO_4$ by $BO_3$ in synthetic minerals (i.e., diopside and forsterite). The bands at 761, 1168, 1259, and 1303 $cm^{-1}$ are consistent with the bands of vibration modes of the $BO_3$ group [22,24,34]. In addition, strong OH band at 3696 $cm^{-1}$ and weaker band at 3593 $cm^{-1}$ are displayed in B-rich forsterite. OH groups commonly exist in nominally anhydrous minerals through a variety of pathways (commonly known as "water") [23,36,37]. Due to the variety and complexity of the infrared spectra of olivine associated with O-H stretching modes, uncertainties remain in the determination of the OH bands associated with the $B(OH)Si_{-1}O_{-1}$ substitution in B-rich olivine. Ingrin et al. [24] presented that the OH bands at 3704 $cm^{-1}$ (//z), 3598 $cm^{-1}$ (//x,y), and 3525 $cm^{-1}$ (//x) are associated with the $B(OH)Si_{-1}O_{-1}$ substitution in synthetic forsterite and natural olivine. Matsyuk and Langer [38] noted that two bands at 3672 and 3535 $cm^{-1}$ are assigned to boron-related defects. Gose et al. [37] speculated that the OH defect at 3597 $cm^{-1}$ may be linked to the coupled $B(OH)Si_{-1}O_{-1}$ substitution. Thus, the OH band at 3593 $cm^{-1}$ is most likely associated with the $B(F, OH)Si_{-1}O_{-1}$ substitution in our B-rich forsterite. The OH band at 3696 $cm^{-1}$ is assigned to OH stretching vibrations of OH defects. Therefore, the IR spectra of B-rich forsterite provided evidence that the incorporation of B into forsterite is mainly caused by the coupled substitution of boron and H for silicon. Theoretically, the ratio of the contents of B to H is close to the 1:1 trend expected from the $B(F, OH)Si_{-1}O_{-1}$ substitution. However, the contents of B (1773.4–1795.91 ppm) in our sample are higher than that of water (1450(300)) wt ppm estimated by Wang et al. [25]. The deviation from the 1:1 trend can be explained by additional fluorine (usually 0.13–0.18 wt% in our sample) [6].

### *4.2. The Rarity of Mg- and B-Rich Forsterite*

The composition of olivine in the mantle and magmatic rocks is typically Fo85~96 [5,39]. Olivine with nearly forsterite end composition is rare and can only be formed in special geological environments. For example, rare forsterite (Fo = 97–99) inclusion in magnesiochromite was reported by Xiong et al. [40], and Majumdar et al. [41] found a pseudomorph rim of Mg-rich olivine (Fo = 98) in serpentinized dunite. Blondes et al. [42] found several olivine grains with Fo at up to 99.8 in multiple primitive basaltic lava flows from Big Pine Volcanic Field (Inyo, CA, USA). Nekrylov et al. [43] reported high-Mg olivine (Fo value up to 99.8) from magnesian skarns and silicate marbles from different locations. In addition, boron-rich olivines are less well-known. Most natural olivine samples have very low concentrations of boron [19,20]. Sykes et al. [22] noted that olivine from the Tayozhnoye iron deposit, Siberia, Russia, contains substantial $B_2O_3$ (1.11–1.35 wt%). Majumdar et al. [41] reported a boron content up to 10.4 ppm in high-magnesium olivine. Nekrylov et al. [43] presented that B concentrations of olivine from magnesian skarns and silicate marbles vary from 23 to 856 ppm. However, the natural forsterite tested in this study surpasses all olivines known in geological objects in magnesium and boron content (Figure 2). The formation of B-rich forsterite remains disputed.

Olivine with high boron content is generally considered to be associated with the metasomatism of boron-rich fluids [22,43]. The B-rich forsterite may be derived from mantle peridotite metasomatized by B-rich fluids. However, the composition of olivine in mantle peridotite is typical $Fo_{86–92}$ [5]. Moreover, mantle olivine has high Ni, Mn, and Co concentrations (Ni, 2040–3310 ppm; Mn, 460–850 ppm; Co, 87–137 ppm) [26]. However, the trace element compositions of B-rich forsterite are evidently inconsistent with the mantle olivine. The above speculation about the origin seems to be incorrect. In addition, Nekrylov et al. [43] presented that olivine from magnesian skarns and silicate marbles are enriched in B and depleted in Ni, Co, and Cr concentrations, which are consistent with our trace element characteristics. According to the description of the geology setting in Wang et al. [25], the formation in which B-rich forsterite forms contains various altered felsic and granitic rocks, dolomitic marble, and serpentinized olivine marble. Moreover, previous study confirms that the formation is a boron-bearing sequence [25]. Thus, we suggest that B-rich forsterite is derived from the metamorphism of magnesian marbles. The origin and formation process of B-rich forsterite needs further study.

## 5. Conclusions

(1) The chemical composition of forsterite from Jian forsterite jade of Jilin province, China, is B-rich end-member forsterite. This forsterite is the most magnesium- and boron-rich natural olivine.

(2) The B-rich forsterite is orthorhombic, in the space group Pnma, and its unit-cell dimensions are: a = 10.1918(7) Å, b = 5.9689(4) Å, c = 4.7484(3) Å, $\alpha = 90°$, $\beta = 90°$, $\gamma = 90°$, and V = 288.86(3) $Å^3$. The unit-cell parameters (a, b, and c) and unit-cell volume of forsterite in Jian forsterite jade are smaller than common natural olivine. There is a negative and significant correlation between unit-cell parameters and Fo values.

(3) The Raman of B-rich forsterite is consistent with that of mantle olivine (Fo = 91). The Raman shift of B-rich forsterite is mainly in 227, 305, 437, 544, 586, 609, 824, 857, 882, 919, and 967 $cm^{-1}$. With the substitution of magnesium for iron increasing in the forsterite-fayalite series, the bands of the Raman spectrum of B-rich forsterite will systematically shift to high Raman shift. The infrared spectrum characteristic peaks of B-rich forsterite appear mainly at approximately 1303, 1259, 1168, 990, 958, 883, 839, 761, 610, 508, 468, and 424 $cm^{-1}$. In particular, the stretching vibrations of BO3 groups occur at 761, 1168, 1259, and 1303 $cm^{-1}$.

**Supplementary Materials:** The following supporting information can be downloaded at: https://www.mdpi.com/article/10.3390/cryst12070975/s1, crystallographic information files (CIF).

**Author Contributions:** Conceptualization, M.H.; methodology, M.H. and B.P.; software, B.P. and S.W.; formal analysis, B.P., S.W. and J.F.; investigation, B.P. and S.W.; data curation, B.P.; writing—original draft preparation, B.P., S.W. and J.F.; writing—review and editing, M.H. and M.Y.; supervision, M.H. and M.Y.; All authors have read and agreed to the published version of the manuscript.

**Funding:** National Mineral Rock and Fossil Specimens Resource Center.

**Institutional Review Board Statement:** Not applicable.

**Informed Consent Statement:** Not applicable.

**Data Availability Statement:** Not applicable.

**Acknowledgments:** We thank Yingliang Jiang and Haiyang Yu from Ji'an Xinli Mining Co, LTD (Jilin, China) for providing samples for this study. We thank Xi Liu and Qiangwei Su for fruitful discussions and suggestions.

**Conflicts of Interest:** The authors declare no conflict of interest.

## References

1. Kadziolka-Gawel, M.; Dulski, M.; Kalinowski, L.; Wojtyniak, M. The effect of gamma irradiation on the structural properties of olivine. *J. Radioanal Nucl. Chem.* **2018**, *317*, 261–268. [CrossRef] [PubMed]
2. Ottonello, G.; Princivalle, F.; Della Giusta, A. Temperature, composition, and f $O_2$ effects on intersite distribution of Mg and $Fe2^+$ in olivines. *Phys. Chem. Miner.* **1990**, *17*, 301–312. [CrossRef]
3. Princivalle, F.; Secco, L. Crystal structure refinement of 13 olivines in the forsterite-fayalite series from volcanic rocks and ultramafic nodules. *Tschermaks Mineral. Petrogr. Mitt.* **1985**, *34*, 105–115. [CrossRef]
4. Shchipalkina, N.V.; Pekov, I.V.; Zubkova, N.V.; Koshlyakova, N.N.; Sidorov, E.G. Natural forsterite strongly enriched by arsenic and phosphorus: Chemistry, crystal structure, crystal morphology and zonation. *Phys. Chem. Miner.* **2019**, *46*, 889–898. [CrossRef]
5. Plechov, P.Y.; Shcherbakov, V.D.; Nekrylov, N.A. Extremely magnesian olivine in igneous rocks. *Russ. Geol. Geophys.* **2018**, *59*, 1702–1717. [CrossRef]
6. Kent, A.J.R.; Rossman, G.R. Hydrogen, lithium, and boron in mantle-derived olivine: The role of coupled substitutions. *Am. Mineral.* **2002**, *87*, 1432–1436. [CrossRef]
7. Müller-Sommer, M.; Hock, R.; Kirfel, A. Rietveld refinement study of the cation distribution in (Co, Mg)-olivine solid solution. *Phys. Chem. Miner.* **1997**, *24*, 17–23. [CrossRef]
8. Nestola, F.; Nimis, P.; Ziberna, L.; Longo, M.; Marzoli, A.; Harris, J.W.; Manghnani, M.H.; Fedortchouk, Y. First crystal-structure determination of olivine in diamond: Composition and implications for provenance in the Earth's mantle. *Earth Planet. Sci. Lett.* **2011**, *305*, 249–255. [CrossRef]

9. Taran, M.N.; Matsyuk, S.S. $Fe^{2+}$, Mg-distribution among non-equivalent structural sites M1 and M2 in natural olivines: An optical spectroscopy study. *Phys. Chem. Miner.* **2013**, *40*, 309–318. [CrossRef]
10. Hazen, R.M. Effects of temperature and pressure on the crystal structure of forsterite. *Am. Mineral.* **1976**, *61*, 1280–1293.
11. Smyth, J.R.; Hazen, R.M. The crystal structure and horhonolite at seeral temperatures up to 900 °C. *Am. Mineral.* **1973**, *58*, 588–593.
12. Xu, J.; Fan, D.; Zhang, D.; Li, B.; Zhou, W.; Dera, P.K. Investigation of the crystal structure of a low water content hydrous olivine to 29.9 GPa: A high-pressure single-crystal X-ray diffraction study. *Am. Mineral.* **2020**, *105*, 1857–1865. [CrossRef]
13. Pamato, M.G.; Nestola, F.; Novella, D.; Smyth, J.R.; Pasqual, D.; Gatta, G.D.; Alvaro, M.; Secco, L. The High-Pressure Structural Evolution of Olivine along the Forsterite—Fayalite Join. *Minerals* **2019**, *9*, 790. [CrossRef]
14. Artioli, G.; Rinaldi, R.; Wilson, C.; Zanazzi, P. High-temperature Fe-Mg cation partitioning in olivine: In-situ single-crystal neutron diffraction study. *Am. Mineral.* **1995**, *80*, 197–200. [CrossRef]
15. Kuebler, K.E.; Jolliff, B.L.; Wang, A.; Haskin, L.A. Extracting olivine (Fo-Fa) compositions from Raman spectral peak positions. *Geochim. Cosmochim. Acta* **2006**, *70*, 6201–6222. [CrossRef]
16. Breitenfeld, L.B.; Dyar, M.D.; Carey, C.J.; Tague, T.J.; Wang, P.; Mullen, T.; Parente, M. Predicting olivine composition using Raman spectroscopy through band shift and multivariate analyses. *Am. Mineral.* **2018**, *103*, 1827–1836. [CrossRef]
17. Yasuzuka, T.; Ishibashi, H.; Arakawa, M.; Yamamoto, J.; Kagi, H. Simultaneous determination of Mg# and residual pressure in olivine using micro-Raman spectroscopy. *J. Mineral. Petrol. Sci.* **2009**, *104*, 395–400. [CrossRef]
18. Bolfan-Casanova, N.; Montagnac, G.; Reynard, B. Measurement of water contents in olivine using Raman spectroscopy. *Am. Mineral.* **2014**, *99*, 149–156. [CrossRef]
19. Marschall, H.R.; Wanless, V.D.; Shimizu, N.; Pogge von Strandmann, P.A.E.; Elliott, T.; Monteleone, B.D. The boron and lithium isotopic composition of mid-ocean ridge basalts and the mantle. *Geochim. Cosmochim. Acta* **2017**, *207*, 102–138. [CrossRef]
20. Ottolini, L.; Le Fèvre, B.; Vannucci, R. Direct assessment of mantle boron and lithium contents and distribution by SIMS analyses of peridotite minerals. *Earth Planet. Sci. Lett.* **2004**, *228*, 19–36. [CrossRef]
21. Grew, E.S.; Pertsev, N.N.; Boronikhin, V.A.; Borisovskiy, S.Y.; Yates, M.G.; Marquez, N. Serendibite in the Tayozhnoye deposit of the Aldan Shield, eastern Siberia, U.S.S.R. *Am. Mineral.* **1991**, *76*, 1061–1080.
22. Sykes, D.; Rossman, G.R.; Veblen, D.R.; Grew, E.S. Enhanced H and F incorporation in borian olivine. *Am. Mineral.* **1994**, *79*, 904–908.
23. Gose, J.; Reichart, P.; Dollinger, G.; Schmadicke, E. Water in natural olivine-determined by proton-proton scattering analysis. *Am. Mineral.* **2008**, *93*, 1613–1619. [CrossRef]
24. Ingrin, J.; Kovacs, I.; Deloule, E.; Balan, E.; Blanchard, M.; Kohn, S.C.; Hermann, J. Identification of hydrogen defects linked to boron substitution in synthetic forsterite and natural olivine. *Am. Mineral.* **2014**, *99*, 2138–2141. [CrossRef]
25. Wang, Y.; He, M.; Yan, W.; Yang, M.; Liu, X. Jianite: Massive Dunite Solely Made of Virtually Pure Forsterite from Ji'an County, Jilin Province, Northeast China. *Minerals* **2020**, *10*, 220. [CrossRef]
26. De Hoog, J.C.M.; Gall, L.; Cornell, D.H. Trace-element geochemistry of mantle olivine and application to mantle petrogenesis and geothermobarometry. *Chem. Geol.* **2010**, *270*, 196–215. [CrossRef]
27. Princivalle, F.; De Min, A.; Lenaz, D.; Scarbolo, M.; Zanetti, A. Ultramafic xenoliths from Damaping (Hannuoba region, NE-China): Petrogenetic implications from crystal chemistry of pyroxenes, olivine and Cr-spinel and trace element content of clinopyroxene. *Lithos* **2014**, *188*, 3–14. [CrossRef]
28. Birle, J.D.; Gibbs, G.V.; Moore, P.B.; ASmith, J.V. Crystal structure of natural olivines. *Am. Mineral.* **1968**, *53*, 807–824.
29. Princivalle, F. Influence of Temperature and Composition on Mg–$Fe^{2+}$ Intracrystalline Distribution in Olivines. *Mineral. Petrol.* **1990**, *43*, 121–129. [CrossRef]
30. Bai, W.; Fang, Q.; Zhang, Z.; Yan, B. Crystal structure and significance of magnesium olivine from pod-shaped chromite from The Lubsha ophiolite in Tibet. *J. Rock Mineral.* **2001**, *20*, 1–10.
31. Chopelas, A. Single crystal Raman spectra of forsterite, fayalite, and monticellite. *Am. Mineral.* **1991**, *76*, 1101–1109.
32. Kolesov, B.A.; Geiger, C.A. A Raman spectroscopic study of Fe–Mg olivines. *Phys. Chem. Miner.* **2004**, *31*, 142–154. [CrossRef]
33. Mouri, T.; Enami, M. Raman spectroscopic study of olivine-group minerals. *J. Mineral. Petrol. Sci.* **2008**, *103*, 100–104. [CrossRef]
34. Halenius, U.; Skogby, H.; Eden, M.; Nazzareni, S.; Kristiansson, P.; Resmark, J. Coordination of boron in nominally boron-free rock forming silicates: Evidence for incorporation of $BO_3$ groups in clinopyroxene. *Geochim. Cosmochim. Acta* **2010**, *74*, 5672–5679. [CrossRef]
35. Guo, Y.X.; Qu, D.l.; Li, Z.; Yang, C.G. Effect of boron oxide on crystal structure and properties of magnesium olivine synthesized from magnesite tailings. *Bull. Chin. Ceram. Soc.* **2016**, *35*, 865–869. [CrossRef]
36. Kovacs, I.; O'Neill, H.S.C.; Hermann, J.; Hauri, E.H. Site-specific infrared O–H absorption coefficients for water substitution into olivine. *Am. Mineral.* **2010**, *95*, 292–299. [CrossRef]
37. Gose, J.; Schmädicke, E.; Markowitz, M.; Beran, A. OH point defects in olivine from Pakistan. *Miner. Petrol.* **2009**, *99*, 105–111. [CrossRef]
38. Matsyuk, S.S.; Langer, K. Hydroxyl in olivines from mantle xenoliths in kimberlites of the Siberian platform. *Contrib. Miner. Petrol.* **2004**, *147*, 413–437. [CrossRef]
39. Sobolev, A.V.; Hofmann, A.W.; Kuzmin, D.V.; Yaxley, G.M.; Arndt, N.T.; Chung, S.L.; Danyushevsky, L.V.; Elliott, T.; Frey, F.A.; Garcia, M.O.; et al. The amount of recycled crust in sources of mantle-derived melts. *Science* **2007**, *316*, 412–417. [CrossRef]

40. Xiong, F.; Yang, J.; Robinson, P.T.; Xu, X.; Liu, Z.; Li, Y.; Li, J.; Chen, S. Origin of podiform chromitite, a new model based on the Luobusa ophiolite, Tibet. *Gondwana Res.* **2015**, *27*, 525–542. [CrossRef]
41. Majumdar, A.S.; Hövelmann, J.; Vollmer, C.; Berndt, J.; Mondal, S.K.; Putnis, A. Formation of Mg-rich Olivine Pseudomorphs in Serpentinized Dunite from the Mesoarchean Nuasahi Massif, Eastern India: Insights into the Evolution of Fluid Composition at the Mineral–Fluid Interface. *J. Petrol.* **2016**, *57*, 3–26. [CrossRef]
42. Blondes, M.S.; Brandon, M.T.; Reiners, P.W.; Page, F.Z.; Kita, N.T. Generation of Forsteritic Olivine (Fo99·8) by Subsolidus Oxidation in Basaltic Flows. *J. Petrol.* **2012**, *53*, 971–984. [CrossRef]
43. Nekrylov, N.; Plechov, P.Y.; Gritsenko, Y.D.; Portnyagin, M.V.; Shcherbakov, V.D.; Aydov, V.A.; Garbe-Schönberg, D. Major and trace element composition of olivine from magnesian skarns and silicate marbles. *Am. Mineral.* **2021**, *106*, 206–215. [CrossRef]